10.2514/6.2015-3436

AIAA AVIATION Forum
22-26 June 2015, Dallas, TX
16th AIAA/ISSMO Multidisciplinary Analysis and Optimization Conference

Aerodynamic Shape Optimization of a Truss-Braced-Wing Aircraft

Davide Ivaldi, * Ney R. Secco, † Song Chen, ‡ John T. Hwang, § Joaquim R. R. A. Martins ¶
University of Michigan, Ann Arbor, Michigan, United States

The truss-braced wing is an aircraft configuration that has the potential to be more efficient than conventional configurations. The coupling between aerodynamics, structures, and propulsion that is present in this configuration significantly increases the complexity of the design, but it offers the potential for a large improvement in performance over the cantilever wing, which we aim to achieve through numerical optimization in this study. Previous studies have primarily used low-fidelity tools that rely on empirical equations or low-order models. Here, we perform high-fidelity aerodynamic shape optimization using the RANS equations with 750 shape and twist design variables. Through optimization, we are able to reduce the drag by more than 28% compared to the baseline geometry, obtaining a final L/D ratio of 25.3, which is a lower than expected value due to high interference drag caused by limited shape design flexibility in the junctions. Despite the limitations, we believe that these results can provide a useful benchmark for future studies involving the truss-braced wing configuration, in addition to revealing insights regarding the complex aerodynamic phenomena associated with this configuration.

I. Introduction

The rapid progress of air travel in the 20th century was an important development that had a positive impact on society. Airliners provide efficient, fast, and safe transportation unmatched by any other means of long distance travel. However, a continuous evolution is required for aircraft to maintain the current trends and avoid threats to air transportation over the coming decades, such as rising fuel costs. Also, due to the growing number of aircraft operating on a daily basis, the optimization of transonic aircraft is becoming more and more important. Even a minor improvement that leads to a small decrease in drag coefficient or aircraft weight can have large benefits in the long run. Indeed, during the last few decades, more and more attention has been paid to reduce aircraft fuel consumption and emissions, and this trend is expected to continue in the years to come.

Over the last 50 years, transonic commercial aircraft have converged upon what appear to be two common solutions: low cantilever wing with either under-wing or fuselage-mounted engines. Clearly, there are some differences that characterize the various aircraft, but it is unlikely that large strides in performance will be possible without a significant change of vehicle configuration. Among all the different, innovative configurations which were suggested in the last 20 years, the truss-braced wing seems to be particularly interesting. In a general sense, the truss-braced configuration adds two structural members to the wing. The first one, which is called main strut, is designed to carry primarily axial loads and joins one point on the wing to a point on the fuselage. The second one, which is called jury strut or vertical strut, connects the main strut and the wing. The concept of the truss-braced-wing configuration dates back to the early 1950s, and it was proposed again by NASA at the beginning of the century as one of the N+3 (2030-2035) generation aircraft concepts. It has been proved that the truss-braced-wing configuration is able to achieve larger reductions in fuel consumption than other unconventional configurations [1, 2].

Aircraft designers have always tried to use high-aspect-ratio wings in order to reduce the lift-induced components of drag. However, many practical issues arise as slender wings can suffer from higher bending and torsional stresses than shorter ones. The coupling of these two modes can also lead to severe consequences, such as the triggering of

*Visiting Scholar, Department of Aerospace Engineering
†Ph.D. Candidate, Department of Aerospace Engineering
‡Visiting Scholar, Department of Aerospace Engineering
§Postdoctoral Research Fellow, Department of Aerospace Engineering
¶Associate Professor, Department of Aerospace Engineering

flutter conditions. The truss-braced wing configuration uses a main strut and a jury strut in order to provide bending load alleviation to the wing, allowing the span to be increased and the wing thickness to be reduced. The longer span reduces the induced drag, while the smaller wing thickness decreases the transonic wave drag, and these two factors increase the aerodynamic efficiency of the overall configuration. The lower wing sweep angle enabled by these reductions in drag provides further drag benefits through larger regions of laminar flow, which is also aided by the lower Reynolds numbers. Decreased weight, along with increased aerodynamic efficiency, in turn permits engine size to be reduced. However, as a first step, in-depth aerodynamic analysis and optimization are required to make sure that the gain obtained by reducing the lift-induced drag is not nullified by the additional parasitic and interference drag generated by the presence of the struts.

Given that the distinguishing feature of the truss-braced wing is the presence of the struts, the focus of this paper is aerodynamic shape optimization of the wing, main strut, and jury strut, with the fuselage and empennage not including in the mesh. In the past, most truss-braced wing studies used low-fidelity models, such as the ones described in [3] and [4]. The premise for this paper is that high-fidelity aerodynamic analysis and optimization are required in order to understand the complex aerodynamic interactions between the wing, the main strut, and the jury strut. This aerodynamic optimization is only the first step of a process that will eventually lead to a multidisciplinary design optimization (MDO) of the full configuration, as the strong synergism between the disciplines previously described is a distinct feature of the truss-braced wing concept.

II. Numerical Tools

The numerical tools used in this aerodynamic shape optimization are the components of the MDO of Aircraft Configurations with High fidelity (MACH) framework and of the Geometric-centric MDO of Aircraft Configurations with High fidelity (GeoMACH) tool suite, both under development in the Multidisciplinary Design Optimization Laboratory (MDO Lab) at the University of Michigan.

A. Geometric Parametrization

The geometry has been created with a parametric geometry modeler which is part of the open-source GeoMACH tool suite [5]. GeoMACH is composed of three different packages: the Parametric Structural Modeler (PSM), the B-spline Surface-modeling Engine (BSE), and the Parametric Geometry Modeler (PGM). In this work, only the last two packages were used in order to create the geometry and manipulate its aerodynamic shape. Therefore, no description will be provided regarding the Parametric Structural Modeler.

In GeoMACH, the aircraft is defined as a Configuration class, which inherits from the base Configuration class for all models of that particular layout and topology. The Configuration instance contains two different types of Component objects: the Primitive class and the Interpolant class. The former is used to represent the basic parts of the airframe, and the latter to smoothly blend surfaces from Primitive components, resulting in a completely watertight geometry. Each Component computes the B-spline control points of its surface, which are then aggregated to define a global control point vector that provide a continuous representation of the aircraft outer mold line. The interpolation of Primitive components enables continuous deformation with differentiability always satisfied. This is one of the main distinguishing features of the geometric modeler, and it is required by the gradient-based optimization algorithms. Indeed, because of this, every component of the computational model must be differentiable and able to provide derivatives of its outputs with respect to its inputs. Furthermore, these derivatives must be computed in an efficient way, and possibly with accuracy to numerical precision. GeoMACH is able to satisfy all of these requirements, and this is the reason why it has been developed and improved over the years. Another important feature of GeoMACH is that it allows to decouple the number of control points and the number of degrees of freedom. In this way, the resolution of geometry representation and manipulation are independent.

One of GeoMACH's features is that it automates the computation of the derivatives of the discrete points describing the geometry with respect to the shape design parameters, as a sparse Jacobian matrix. Internally, GeoMACH simplifies the implementation of this computation using two techniques. First, it decomposes the function mapping the design parameters to the points on the geometry as a sequence of smaller operations with the nonlinearity of the overall mapping contained in only two of these smaller operations. Each of these operations acts on global vectors that concatenate the contributions from all the aircraft components—e.g., the B-spline control points from the wing,

fuselage, tail, and other components are combined into a single vector. The sparse Jacobians for each of these smaller operations are computed and then combined together using the chain rule. The second technique is the allocation of two 1-D arrays for each of the global vectors. The first one contains the actual data and the second one contains the global index of each entry. Therefore, if a given component—e.g., the wing—owns a pointer to its local part of a global vector, it also owns a pointer to its part of the index array, so that for each value, it knows the corresponding index in the global vector without knowing any information about the other components. A more detailed description of the GeoMACH tool, with all its packages can be found in Hwang et al. [5, 6]

Figure 1 shows an example of a full truss-braced-wing configuration generated by GeoMACH. The manipulation of the CFD surface mesh is made possible using a routine inside GeoMACH that computes the projection of the CFD surface mesh points on the geometry surface, finding the closest surface point. Generally, the mesh points lies on the surface and the projection is trivial. However in some cases, especially when dealing with complex geometries, the perfect association between mesh points and surfaces can be more difficult. In these cases, GeoMACH stores displacement vectors representing the difference between the mesh points and the closest surface points, and then when the surface is updated, it applies the change to the surfaces and adds back the displacement vectors, in order to compute the new positions of the mesh points.

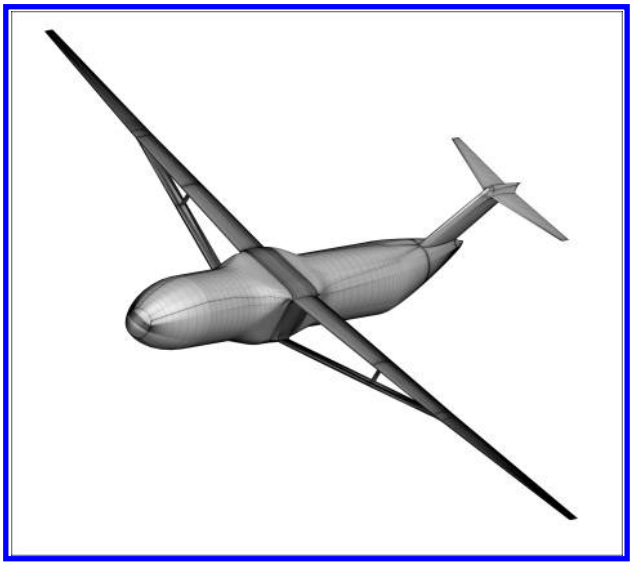

Figure 1. View of the full truss-braced wing configuration generated by GeoMACH.

Beyond the results of the optimization of the truss-braced wing configuration, which will be described in Section IV, another outcome of this study is the addition of two features in GeoMACH. First of all, the definition of the displacement vectors aforementioned allows to extend the use of GeoMACH also to complex or unconventional configuration, as, for instance, the truss-braced wing one. Without this solution, the projection of the mesh points on the surface, performed by GeoMACH even before the first iteration in the optimization process, could have created some negative volumes which would have made impossible to start with the optimization process itself. The second feature implemented was the possibility to create blunt trailing edges. Previously, GeoMACH had only been used for Euler-based optimizations, so only sharp trailing edges were required.

B. Mesh Perturbation

The mesh deformation algorithm is required to alter the mesh for CFD analysis to match the geometry modified by the optimizer. In order to perform this matching, the volume mesh is required to move in such a way that the surface mesh matches the updated geometry and that the quality of the mesh itself is degraded as little as possible. The mesh perturbation scheme used in this work is a novel mesh deformation model for unstructured meshes which has been developed using a tree-code optimization of a direct interpolation method [7]. This mesh perturbation algorithm was

implemented by Dr. Gaetan Kenway.

The key methodology of this mesh warping scheme is to utilize an inverse distance weighting function to interpolate each grid node displacement, which can handle both translation and rotation, and preserve high mesh quality near the body to resolve the boundary layer. Moreover, this scheme can also support large deformations before the mesh regeneration would be required. This algorithm demonstrates good parallel performance, and since this scheme works for unstructured meshes, it also works for the structured meshes employed in this work.

C. CFD Solver

The flow solver used is the Stanford University multiblock (SUMad) [8]. SUMad is a finite-volume, cell-centered multiblock solver for the compressible Euler, laminar Navier-Stokes, and Reynolds-Averaged Navier-Stokes equations (steady, unsteady, and time-periodic), and it was initially developed at Stanford University under the sponsorship of the Department of Energy Advanced Strategic Computing (ASC) initiative. The aforementioned types of equations supported by SUMad are solved on multi-block structured mesh. A Python interface is available, which makes SUMad suitable for use in multidisciplinary environments in conjunction with other tools. The main flow is solved using both an explicit multi-stage Runge–Kutta method and a recently implemented preconditioned matrix-free Newton–Krylov approach, along with geometric multi-grid. This implementation of the matrix-free Newton–Krylov method solves the nonlinear system using a finite-difference approximation for the Jacobian-vector products and a Krylov subspace method to solve the Newton correction equations [9] with superlinear convergence. A segregated Spalart-Allmaras turbulence equation [10] is iterated with the diagonally dominant alternating direction implicit (DDADI) method.

To efficiently compute the gradients required for the optimization, a discrete adjoint method developed and implemented for the Euler and RANS equations within SUMad in the MDOlab has been used. This adjoint implementation supports both the full-turbulence and frozen-turbulence models, but in the present work only the full-turbulence model has been used. The adjoint equations are always solved with preconditioned GMRES [11] using PETSc.

Summing up, in this work we solved the RANS equations and applied the discrete adjoint method to compute the gradients required for optimization. The choice of using RANS equations comes from the analysis of the results of many Euler-based aerodynamic shape optimizations performed in the Multidisciplinary Design Optimization Laboratory (MDOlab) at the University of Michigan. Indeed, due to the missing viscous effects, serious issues have been observed with the resulting optimal Euler-based designs. While Euler-based optimization can provide design insights, these design are usually significantly different from those obtained with RANS. For this reason, we decided for this study to perform a RANS-based optimization of the truss-braced wing configuration, in order to achieve a more realistic design.

D. Optimization Algorithm

The optimization algorithm used for this work is SNOPT (Sparse Non-linear Optimizer) [12] through the Python interface pyOptSparse, which is a modification to the original pyOpt framework [13]. SNOPT is a gradient-based optimizer that implements the sequential quadratic programming method; it is capable of solving large-scale nonlinear optimization problems with thousands of constraints and design variables. In a very general sense, the form of the constrained non-linear optimization problems solved by SNOPT is the following,

$$\begin{aligned} \text{minimize} \quad & f(x) \\ \text{with respect to} \quad & x \\ \text{subject to} \quad & g_{j_L} \leq g_j(x) \leq g_{j_U},\ j = 1,...,m \\ & x_{i_L} \leq x_i \leq x_{i_U},\ i = 1,...,n \end{aligned}$$

where x is the vector containing the n design variables, $f(x)$ is a non-linear function, and $g(x)$ is a set of m non-linear functions. In order to solve this kind of problems, SNOPT uses a smooth augmented Lagrangian merit function, and the Hessian of the Lagrangian is approximated using a limited-memory quasi-Newton method. SNOPT is combined with a discrete adjoint gradient evaluations method to solve the problem efficiently. The choice of using a gradient-based optimizer comes from the unfeasibility of using gradient-free methods, such as genetic algorithms. These methods have slower convergence rates, and the large number of functions evaluations make them inappropriate for aerodynamic shape optimization problems with high number of design variables, given current computational resources.

III. Problem Formulation

The optimization problem we solve in this study is lift-constrained drag minimization of a truss-braced wing configuration based on the 765-095-TS1 Truss-Braced Wing of the Boeing Sugar project [14]. In this section we provide a complete description of the problem.

A. Baseline Geometry

The baseline geometry which was used as a starting point for the optimization is inspired by the 765-095-TS1 Truss-Braced Wing of the Boeing Sugar project [14]. The geometric characteristics are shown in Table 1. The truss-braced wing itself is shown in Figures 2, 3, 4, and 5.

GEOMETRIC CHARACTERISTICS	
WING	
AREA $[m^2]$	125
ASPECT RATIO	21.44
SPAN $[m]$	51.80
TAPER RATIO	0.328
MAC $[m]$	2.522
DIHEDRAL $[deg]$	-1.70
$1/4$ CHORD SWEEP $[deg]$	12.55
ROOT CHORD $[m]$	3.387
TIP CHORD $[m]$	1.111
MAIN STRUT	
ASPECT RATIO	9.81
SPAN $[m]$	15.20
TAPER RATIO	1.00
MAC $[m]$	1.55
DIHEDRAL $[deg]$	15.00
$1/4$ CHORD SWEEP $[deg]$	5.60
ROOT CHORD $[m]$	1.55
TIP CHORD $[m]$	1.55
JURY STRUT	
ASPECT RATIO	1.78
SPAN $[m]$	1.46
TAPER RATIO	1.00
MAC $[m]$	0.82
ROOT CHORD $[m]$	0.82
TIP CHORD $[m]$	0.82

Table 1. Geometric characteristics of the baseline truss-braced wing configuration.

The most striking geometric characteristic of the truss-braced wing configuration is certainly the very high aspect ratio. For comparison, a Boeing 737-900ER, which has almost the same overall length (42.6 m for the truss-braced wing and 42.1 m for the Boeing 737-900ER), has a wingspan of 35.7 m and a wing aspect ratio of 9.45, which is less than half the wing aspect ratio of the truss-braced wing configuration. The main strut is reasonably big as its chord (which is the same at the root and at the tip) is 61.5% of the mean aerodynamic chord of the wing. The main strut is slightly swept, has no taper, and has a significant dihedral angle. The intersection between the main strut and the wing occurs at 58.7% of the wingspan. The jury strut is certainly smaller, as its chord is only 32.5% of the mean aerodynamic chord of the wing, and it is also not tapered. The jury span is small compared to the other surfaces, and both the dihedral and sweep angles are null. The intersections of the jury strut with both the wing and main strut occur

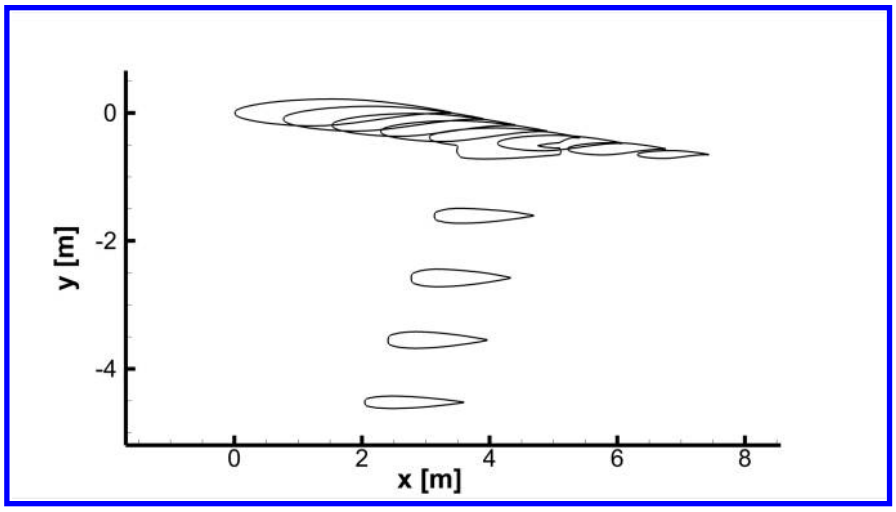

Figure 2. Side view of the truss-braced wing configuration.

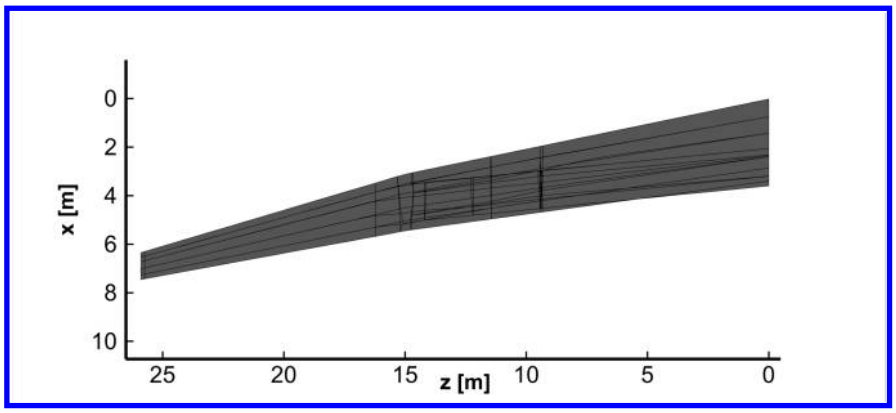

Figure 3. Top view of the truss-braced wing configuration.

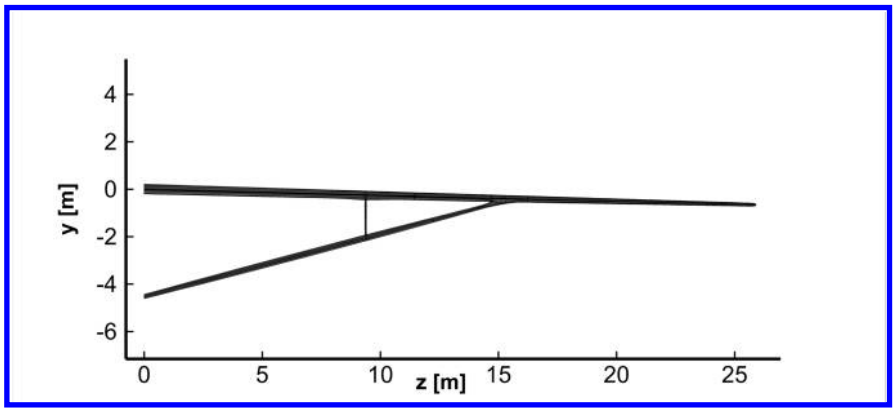

Figure 4. Front view of the truss-braced wing configuration.

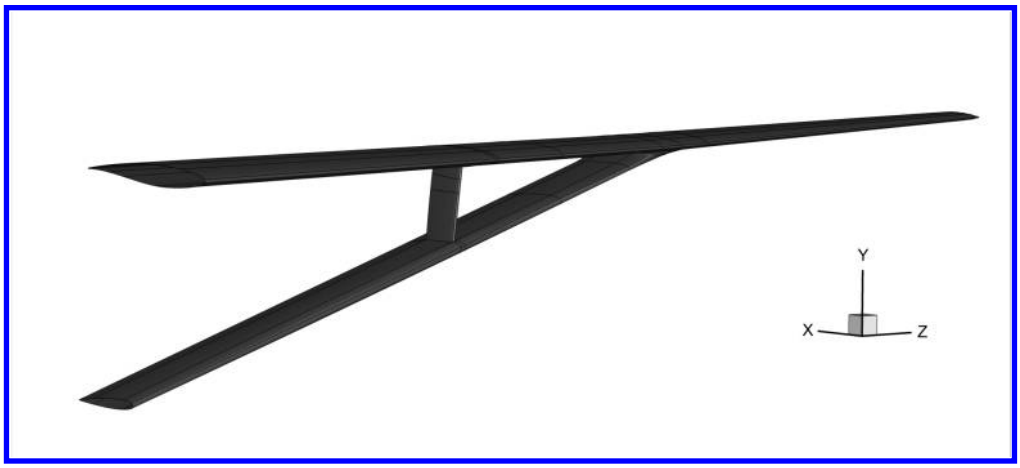

Figure 5. Three-dimensional view of the truss-braced wing configuration.

at 36.2% of the wingspan.

B. Mesh generation

After the definition of the geometry, the mesh required for the optimization was generated. This was one of the most challenging steps of the entire process because of the unconventional geometry of the truss-braced wing. The particular configuration of this kind of wing required a careful definition of the topology and a proper splitting of the mesh blocks. Especially, the triangular area between the wing, the main strut, and the jury strut represented a serious issue. Indeed, in this area, it was very difficult to have all quadrangular, high-quality elements. Figure 6 shows an instance of the surface mesh in this intersection.

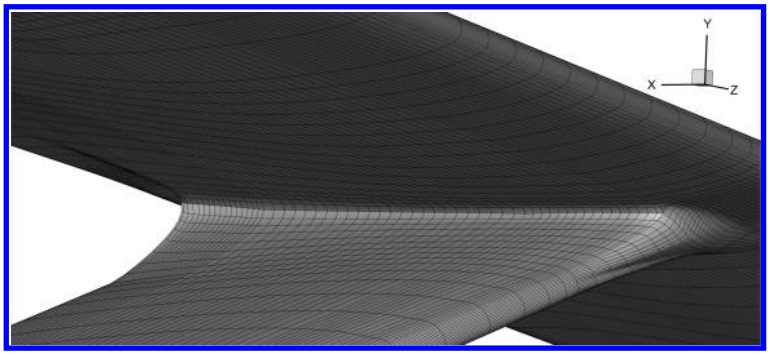

Figure 6. Surface mesh in the wing-main strut junction of the truss-braced wing.

The number of surface nodes on every block edge was chosen using only multi-grid friendly numbers; that is on every edge the number of nodes was given by $2^n m + 1$, where both n and m are integers. This allowed us to accelerate the analysis steps using the multi-grid method. Eventually, the complete volume mesh was created using a geometric law in the off-wall direction, and the boundaries condition were applied. The final mesh has a little more than 2 million cells and during the optimization it was coarsened four levels down to a mesh with only 4309 cells in order to perform a multi-grid optimization and speed up the convergence of the SUMad analysis. We also note that a finer mesh with more than 16 millions cells was also created in order to perform a more precise analysis on the truss-braced wing configuration. However, because of the computational cost and time required, we only used this mesh for verification purposes and not for optimization.

C. Optimization Problem Formulation

The goal of this optimization is to minimize the drag coefficient by varying the design variables defined in GeoMACH and given to the optimizer. Since we are performing an aerodynamic shape optimization, structural members are not considered, and therefore stresses and strains due to aerodynamic loads are not computed. Also, the wing planform is fixed, which means that the optimizer is not allowed to change the span, chords, and dihedral of the components. Regarding the wingspan, if it had been defined as a design variable and let free to change, almost certainly the optimizer would have provided an optimized configuration with a very large span, unfeasible from the structural point of view.

An important set of constraints that must be imposed is bounds on the airfoils' thicknesses. Without these constraints and the consideration of structural members, the optimizer would certainly try to reduce the thickness as much as possible to reduce the parasite and wave drag. It is also important to underline that, often, in aerodynamic shape optimization 100% thickness constraints are used. The reason for this is that the baseline configuration is usually created with a CAD software, therefore being very close to an already existing geometry which has been designed considering the structural members so that it resists to stresses and strains generated by aerodynamic loads. Since decreasing the thickness can cause structural issues, the optimizer is only free to shift a given chordwise position of the airfoil up and down, modifying the camber but not the thickness.

In this optimization, 80% thickness constraints were used. Indeed, the geometry of the truss-braced wing has been created with GeoMACH, which is able to create a completely smooth C^1 surface, but it is not able to exactly match an already existing geometry (also because this is not its purpose). Therefore, the thickness of the airfoils is bigger than in the real case. Also, one of the advantages of the truss-braced wing is the possibility of using the main strut and the jury strut to alleviate the bending load of the wing. This allows to reduce the thickness of the wing itself with respect to a conventional cantilever wing, bringing a benefit especially in terms of parasite drag. Nevertheless, no structural analysis has been performed in this study, therefore we can not get the information about the maximum thickness decrease allowed by the presence of the struts and we have to guess a reasonable value. This situation underlines once more the importance of the aerostructural optimization as the only possibility to completely understand the potential benefits of the truss-braced wing configuration.

We relied on the results of previous low-fidelity optimization studies to estimate values for the thickness constraints. Gundlach et al. [3] suggest that the optimized configuration, obtained with the goal of minimizing the take-off gross weight (TOGW), should have a thickness-to-chord ratio (t/c) of 14.37% at the root and 6.56% at the tip. We can therefore estimate that the average t/c should be around 10.5%. Gur et al. [2] also optimized a truss-braced wing aircraft to minimize TOGW, and the optimum configuration has a centerline thickness-to-chord ratio of 9.7% and a tip thickness-to-chord ratio of 10.3%. On the other hand, using the fuel consumption as the objective function, the same authors suggest an optimized configuration with a centerline thickness-to-chord ratio of 8.7% and a tip thickness-to-chord ratio of 7.8%. Meadows et al. [15], with their TOGW-driven optimization, suggest an optimized configuration with a root thickness-to-chord ratio of 5.18% and a tip thickness-to-chord ratio of 8.57%. Grasmeyer [4] suggests a strut-braced wing optimized configuration with a centerline thickness-to-chord ratio of 11.9% and a tip thickness-to-chord ratio of 5.0%. All the results considered current technologies with current-generation materials and so on.

Now, considering that the RAE2822, which is the airfoil used for the baseline wing, has a thickness-to-chord ratio of 12.1%, it is clear that there is room for reducing this value. However, we did not want to reduce this value too much, therefore a 20% maximum reduction of the thickness-to-chord ratio seemed to be a proper value. Indeed, using this value, the t/c ratio can decrease at most down to 9.7%, which is a value in line with those previously shown. It should also be underlined that the reduction in the t/c ratio is obtained only reducing the thickness, as the chord is fixed for the whole wing.

This same thinking applies to the main strut and the jury strut. They were created using as original airfoils the NACA0012 and the NACA0010, respectively (we note that the leading edge is thickened when GeoMACH performs a fit of the NACA airfoils because of an insufficient number of control points, but this is easily fixed). However, as they are only supporting elements because the main loads should be carried by the wing, their thickness can be decreased further. Therefore, for these components, we chose 75% percent thickness constraint. This means that the main strut thickness-to-chord ratio can be decreased at most down to 9%, and the jury strut thickness-to-chord ratio down to 7.5%.

A couple of exceptions to these general thickness constraints must be applied. First of all, the trailing edge

thickness must remain constant. In fact, the degrees of freedom around the trailing edge are not allowed to move at all. This choice was made because usually the trailing edge is already thin enough so that its thickness can not be further reduced. Also, a movement of the trailing edge can cause some mesh issues. The trailing edge is a delicate zone for both the surface and the volume meshes, therefore preventing any shape modification at the trailing edge may prevent the development of negative volumes. The second exception is the area surrounding the junctions. Like the trailing edge, these are very delicate zones and, for the same reasons, they are not allowed to decrease their thicknesses. One of the possible future developments of the truss-braced wing project is to perform a detailed optimization of the junctions through a different approach, as will be explained in Section V.

In this study, the thickness constraints are enforced over 20 chordwise positions in 23 spanwise sections of the wing, over 8 chordwise positions in 14 spanwise sections of the main strut, and over 5 chordwise positions in 10 spanwise sections of the jury strut, totaling 622 thickness constraints. The last constraint enforced is the lift constraint, given by $C_L = 0.775$.

Regarding the design variables, in this study we used shape and twist design variables. The shape design variables are B-spline control points defined in GeoMACH which are able to move up and down, modifying the thickness and the camber of the airfoil. The twist design variables are used to modify the span-wise airfoil twist with the ability to achieve a constant twist, linear twist, piecewise, or a B-spline twist distribution. In principle, the twist could be modified using just shape design variables. However, in our experience, the final results obtained by using shape-only design variables and the ones given by shape-twist design variables slightly differ. Indeed, the shear twist produced by shape design variables is not exactly the same one usually generated by twist design variables. The angle of attack of the entire configuration is one additional design variable which is important to match the lift constraint. Table 2 summarizes the number and distribution of the design variables. Overall, we have an optimization problem whose goal is to minimize the drag coefficient using 751 design variables and subject to 623 constraints.

FLIGHT CONDITION DESIGN VARIABLES				
Angle of attack				1
TOTAL FLIGHT CONDITION DESIGN VARIABLES				1
SHAPE DESIGN VARIABLES				
COMPONENT	**SURFACE**	**CHORDWISE POSITIONS**	**SPANWISE SECTIONS**	**TOTAL NUMBER**
Wing	Upper	15	12	180
Wing	Lower	15	12	180
Main Strut	Upper	12	10	120
Main Strut	Lower	12	10	120
Jury Strut	Upper	10	6	60
Jury Strut	Lower	10	6	60
TOTAL SHAPE DESIGN VARIABLES				720
TWIST DESIGN VARIABLES				
COMPONENT				**TOTAL NUMBER**
Wing				20
Main Strut				10
TOTAL TWIST DESIGN VARIABLES				30
GLOBAL NUMBER OF DESIGN VARIABLES				751

Table 2. Design variables used for the aerodynamic shape optimization of the truss-braced wing.

The optimization was performed using 64 processors, and it took about 30 hours. The CFL number chosen for the simulation was 1.5. The desired convergence factor, which is taken relative to the initial residual on the fine grid,

was set equal to 10^{-10}, which is a very low convergence level. The possibility to reach such a strict convergence is given by the use of the Newton–Krylov solver. The relative tolerance that has been set in order to define the value of the residuals at which SUMad switches to the Newton–Krylov solver is 10^{-6}. This means that the residuals must be 10^{-6} times smaller than their value at the beginning of the analysis on the coarse mesh for the Newton–Krylov solver to start.

The convergence level of the adjoint solver is equal to 10^{-7}. The approximate Jacobian was used, as well as the automatic differentiation for the preconditioning matrix. Also, in this matrix, the cross derivative terms were kept. The global preconditioner chosen was the Additive Schwartz, whereas, on the local preconditioning iterations, an Incomplete LU factorization was used.

Eventually, the aerodynamic parameters used for the simulation are shown in Table 3.

Mach	0.73
$C_{L_{target}}$	0.775
Altitude $[m]$	13411
Wing Area $[m^2]$	62.5
MAC $[m]$	2.522

Table 3. Flight conditions and geometric characteristics required by SUMad for the optimization.

IV. Aerodynamic Shape Optimization

In this section, the results of the aerodynamic shape optimization of the truss-braced wing are presented and discussed. The optimization history is shown in Fig. 7 while Tab. 4 compares the aerodynamic characteristics of the baseline and the optimized configurations. The drag is reduced by more than 28% after the optimization process. The optimized L/D ratio of 25.3 is low considering the fuselage and empennage are not included, but it represents an improvement over the baseline nonetheless.

Parameter	**Baseline**	**Optimized**
α [deg]	$\alpha = 3.385^\circ$	$\alpha = 2.753^\circ$
C_L	0.775	0.775
C_D	0.04288	0.03059
L/D	18.07	25.33

Table 4. Comparison of aerodynamic characteristics between the baseline and optimized configurations. The aerodynamic efficiency increased by 40%.

The pressure coefficient contour lines on the upper surface of the wing are plotted in Figure 8. Clearly, the optimizer is able to distribute these lines in a more even manner, but the contours at the root, especially in the fore part of the wing, are neither parallel nor evenly spaced. Moving toward the tip of the wing, the lines become parallel but, especially in the sections close to the junction with the main strut, they are very dense at the mid-chord position. This situation clearly indicates the presence of a shock that extends almost up to the wing tip, as can be seen also from the middle and bottom pictures, where the shock is highlighted. The contour lines are now less dense than in the baseline configuration, indicating that the shock is weaker for the optimized configuration. However, its presence is a clear sign that the optimizer is not able to shape the geometry fully.

The most significant result in this optimization is the elimination of the shock in the triangular area between the wing, main strut, and jury strut. Morever, the shock has been reduced on the upper surface of the wing between the root and the intersection with the jury strut, and an improvement can be seen also on the upper surface of the strut. Globally, it can be surmised that the inability of the optimizer to modify the twist of the wing and the main strut around the intersections, also affected the twist optimization in nearby areas. Moreover, this situation generated some mesh failures that stopped the optimization before it was completely converged.

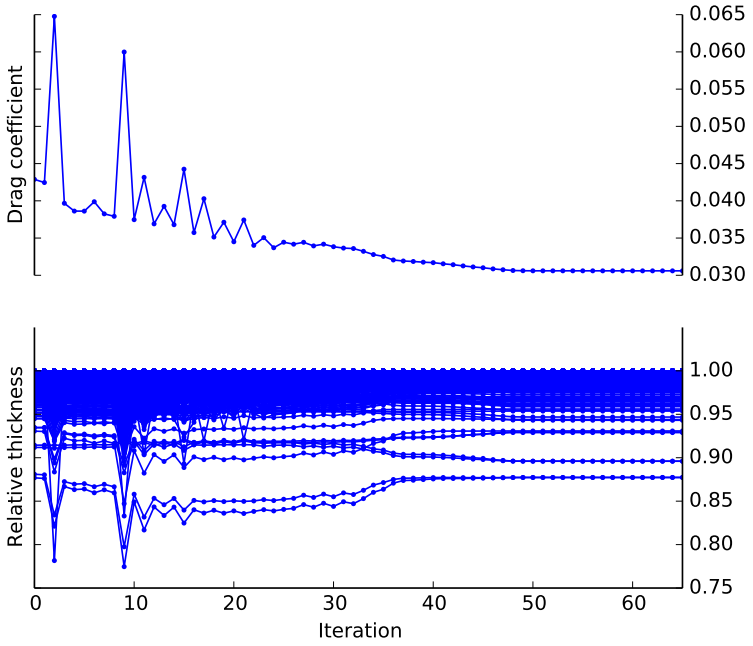

Figure 7. Optimization history. The thicknesses were not reduced below the 80% threshold.

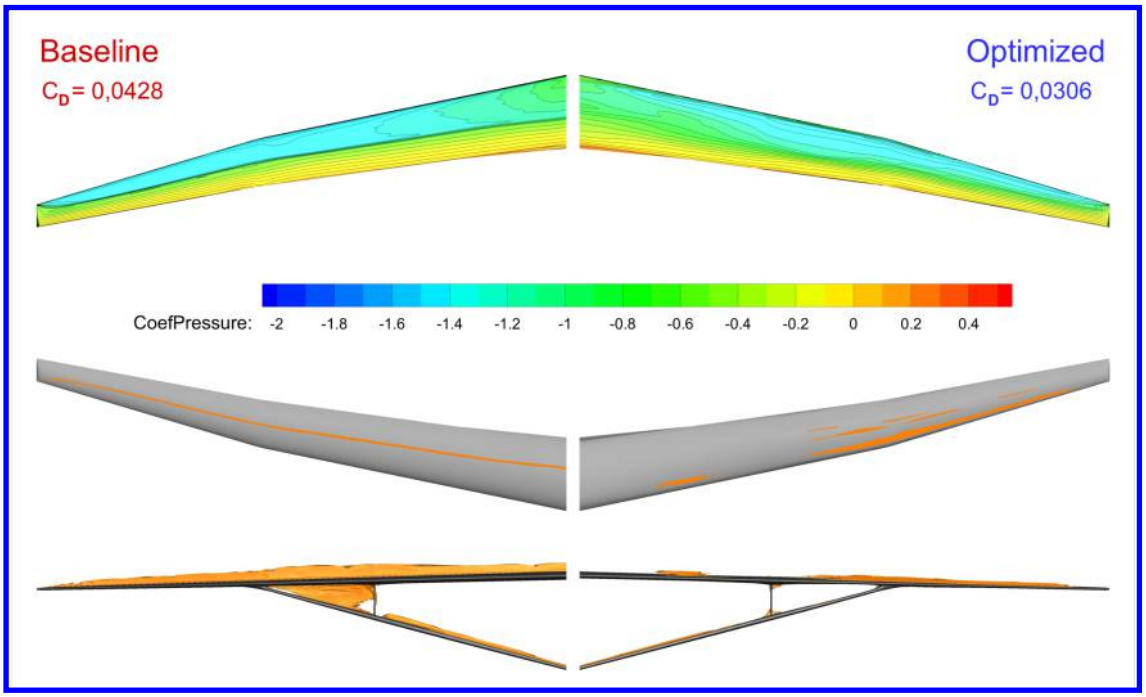

Figure 8. Distribution of the C_p on the upper surface of the wing (top) and shock distribution (middle and bottom).

The evolution of the pressure and the shape of the optimized airfoil are shown in Figure 9. These three airfoils are located at 22.36%, 48.79%, and 75.22% of the semi-span respectively. The C_p distribution is now much smoother in the optimized configuration as compared to the baseline one. A shock can still be seen in the second airfoil around the mid-chord position, and in the third airfoil, immediately after the leading edge. However, these shocks are much weaker than the ones in the baseline configuration. The shape of the first and third airfoils are slightly different compared to the baseline airfoils, with the biggest difference being on the lower surface, which moved upward in order to reduce the thickness. However, the optimizer does not hit the lower bound of 80% of the initial thickness in either of these two airfoils. The situation is different in the second airfoil. In the baseline configuration, the optimizer had to considerably modify the airfoil shape in order to achieve a smoother pressure distribution. Both the upper and lower surfaces moved upward, but the biggest difference is in the lower one, which is now almost completely flat. Furthermore, the thickness reduction was much more significant in this section.

Looking at the pressure coefficient contour lines on the upper surface of the main strut, shown in Figure 10, it is immediately clear the best improvement has been achieved in the triangular zone included between the intersections with the jury strut and the wing. Indeed, the shock nearly disappeared in this area, even though the contour lines are neither parallel nor evenly spaced. On the inner surface of the jury strut, the pressure coefficient contour lines are now more evenly distributed, and there is no shock anymore at the mid-span position. However, it appears that the shock moved closer to the upper and lower junctions. Close to the root on the upper surface of the main strut, the C_p contours show several differences from the baseline. The shock moved toward the leading edge and appears to be weaker than the one in the baseline configuration. The contour lines are more evenly distributed at the root section, but as we move closer to the junction with the jury strut, this distribution becomes irregular. Again, the problem is that in this zone, because of the mesh failures, the optimizer is unable to twist the main strut, and therefore the geometry around the intersection is not completely optimized.

One more observation can be made about the strut by looking at the airfoils shown in Fig. 11. These strut sections are located at planes taken at 22.36% and 48.79% of the wing-span, respectively. This means that the first one is between the root and the wing-jury junction, and the second one is between the wing-jury junction and the strut-wing junction. The shape of the second airfoil is only slightly changed, with both upper and lower surfaces moved downward. Especially, the upper surface is now flatter. However, the real change with the respect to shape can be seen in the first airfoil. In this case, the optimizer considerably modified the shape of the upper surface, moving it downward.

Another interesting result is shown in Fig. 12. This figure shows the pressure coefficient contour lines in the volume around the same two span-wise locations previously defined, which are at 22.36% and 48.79% of the semi-span, respectively. In both sections the shock moved toward the leading edge and it became weaker as a result of the optimization. But the second section underwent more significant changes. At this location we had a very strong shock covering the whole area between the wing and the main strut in the baseline configuration, which is caused

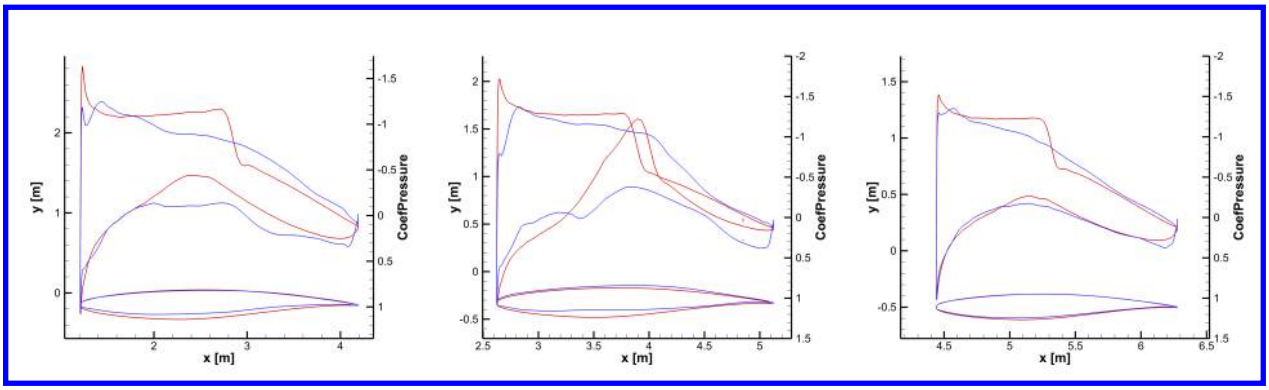

Figure 9. Distribution of the C_p at three different sections of the wing: comparison between the baseline (red) and optimized (blue) configurations.

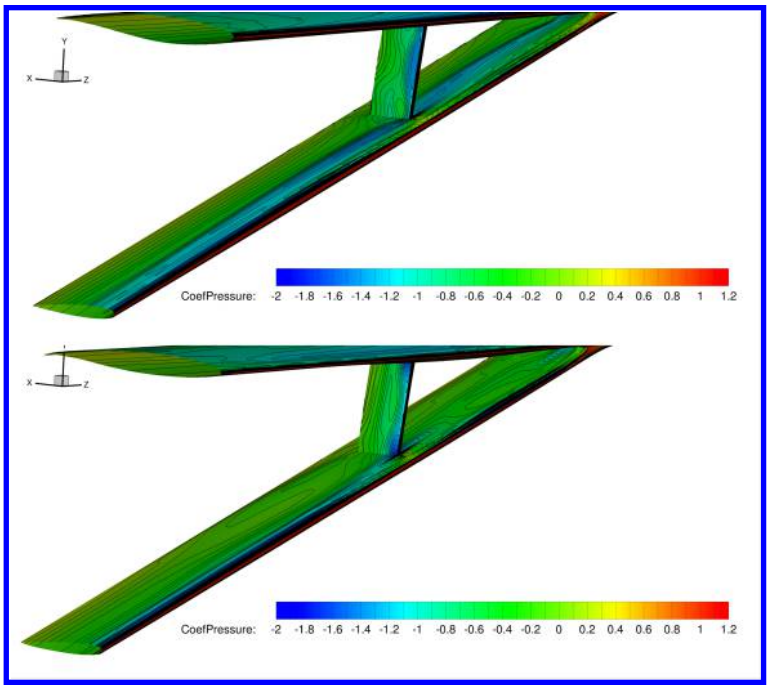

Figure 10. Three-dimensional view showing the C_p distribution on the upper surface of the main strut and on the inner surface of the jury strut: comparison between the baseline (top) and optimized (bottom) configurations.

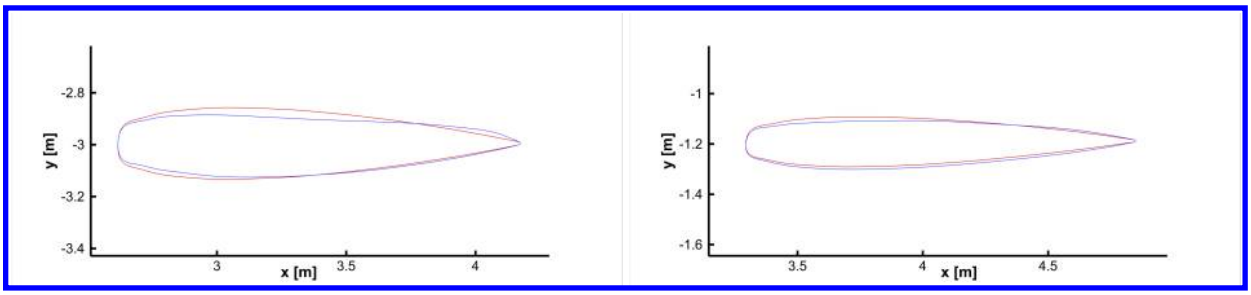

22.36% semi-span 48.79% semi-span

Figure 11. Airfoil shape of the strut at two different sections: comparison between the baseline (red) and optimized (blue) configurations.

by what it seems to be a convergent-divergent nozzle generated by the camber on the upper surface of the main strut and the lower surface of the wing. Now, in the optimized configuration, the optimizer tried to eliminate this situation by moving downward the upper surface of the main strut and moving upward the lower surface of the wing, creating some sort of constant section duct. The result is that there is almost no shock anymore in this area, and the pressure is rather constant. One last insight that can be obtained by the analysis of this figure regards the pressure distribution on the main strut. Indeed, the previous guess regarding the negative lift in the inner section can be confirmed, as the strut experiences a lower pressure on the lower surface.

According to the optimizer, therefore, the penalty paid in terms of induced drag by increasing the lift generated by the wing (which now also has to compensate for the negative lift produced by the main strut) is more than compensated by the disappearing of the shock in the area included between the wing and the main strut, and thus by the reduction of wave drag. Furthermore, this result is very similar to the ones found on previous studies ([6] and [16]) that used Euler equations as aerodynamic model, which also suggests that the negative lift on the main strut results from the trade-off between induced drag and wave drag.

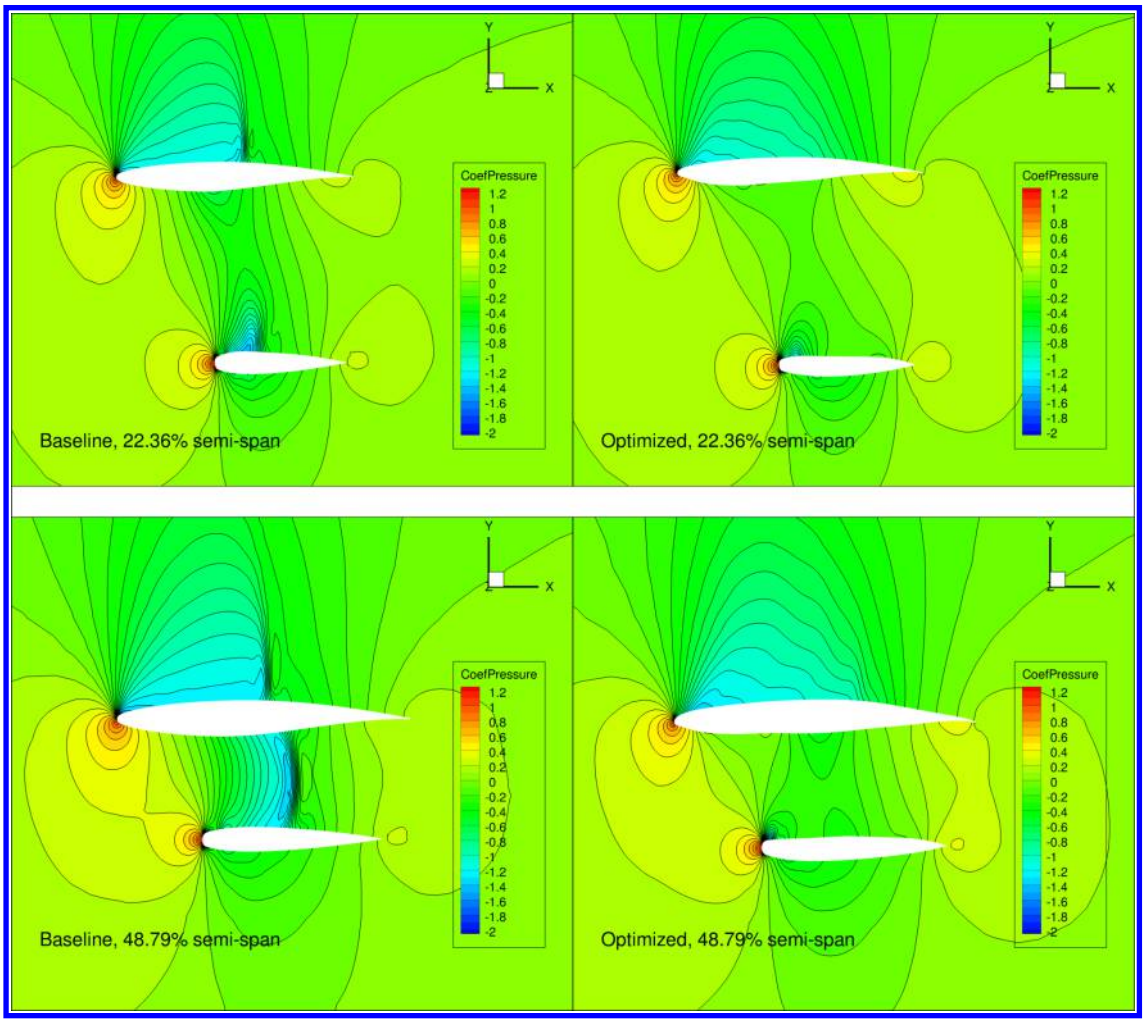

Figure 12. Distribution of the C_p in the volume around two sections of the truss-braced wing: comparison between the baseline (left) and optimized (right) configurations.

The overall C_l spanwise distribution is shown in Figure 13. The optimizer tried to make the lift distribution as close as possible to the elliptical one by reducing the lift generated by the sections close to the root and increasing the lift in the sections located around the intersection between the wing and the main strut. However, because of the impossibility to modify the twist in the sections around the junctions, the optimizer was not able to make this distribution close to elliptical.

Finally, the velocity streamlines and separation reversed-flow regions around the main strut-wing junction are shown in Figure 14. The very odd shape of this junction, which was not modified by the optimizer because of the lack of design variables in this area, creates a region of stagnation and also reverse flow. In the figure on the left, the shape of velocity streamlines indicates that, especially at the wing-strut junction and on the jury-strut junction, the flow does not move straight, but it changes its direction and goes the other way round toward the leading edge. The reverse flow zones are indicated in red in the picture on the right, where it is shown that they occupy almost the whole trailing edge and junctions.

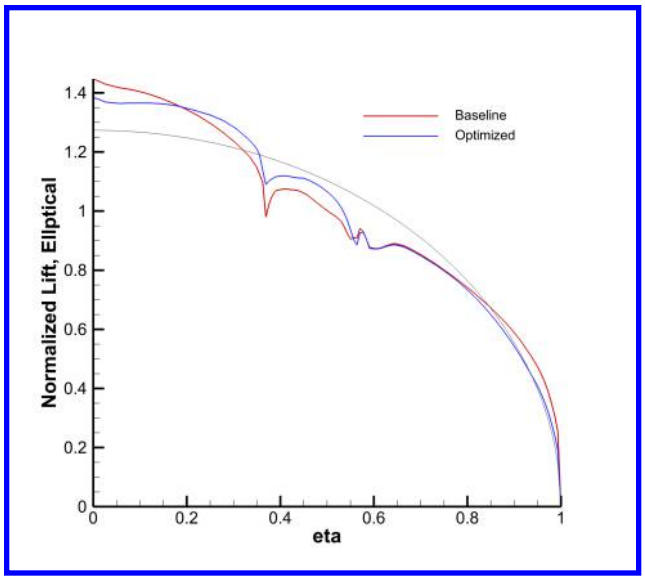

Figure 13. Spanwise distribution of the C_l: comparison between the baseline (red) and optimized (blue) configurations.

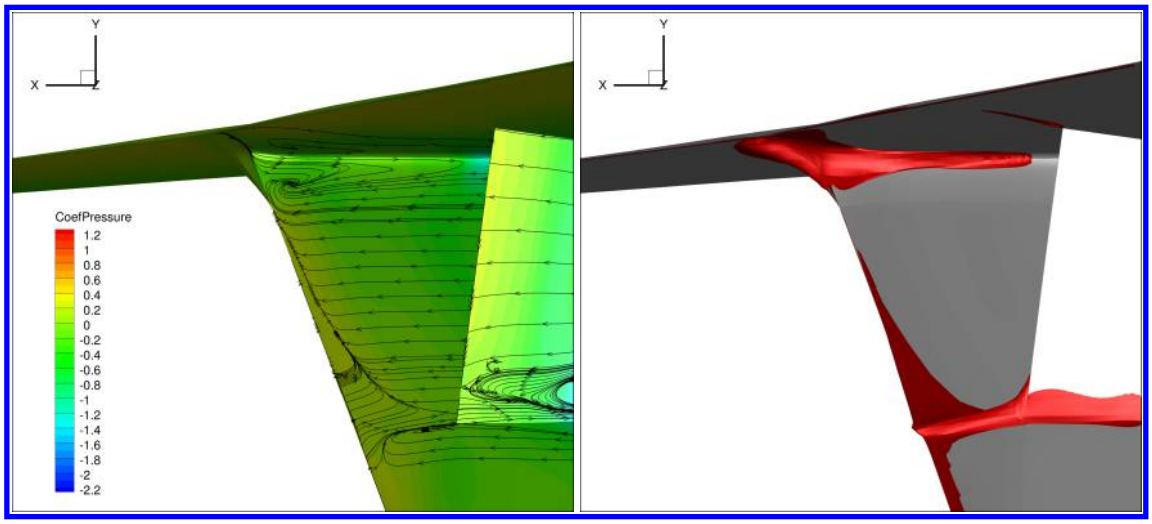

Figure 14. Streamlines at the intersection of the main strut with the jury strut and the wing (left) and zones of reverse flow (bottom) indicated in red.

V. Conclusion

The results shown in the previous section do not meet our expectations because the final L/D ratio of 25.3 is still lower than that of modern conventional wings at cruise conditions. Therefore, by looking at these results without considering the limitations of the model used, one could say that the conventional wing is still better in terms of performance than the truss-braced wing. However, the limitations of this study present us from making such a conclusion.

The first limitation of the study presented here is the baseline geometry created with GeoMACH. By using this tool, the junctions are created almost completely automatically in order to connect different components and to define a watertight geometry with completely smooth C^1 surfaces. However, there is room for improvement in terms of the smoothness of the junctions in the baseline geometry.

The second limitation, which is related to the first one and has already been described throughout this paper, is the lack of design variables on the junctions. The results presented in this paper only parametrize the shapes of the wing and struts with no freedom manipulate the local shape within the junctions. Junction shape variables have recently been implemented and will be included in the optimizations in future work.

The third limitation is the mesh quality. The mesh created and used for this study originally had more than 16 million cells. However, because of the computational time which would have been required to complete the optimization using such a big mesh, we decided to coarsen that mesh one level down, and to use a mesh with 2 millions cells as the finest mesh for the optimization. However, the aerodynamic analysis performed with 2 millions cells mesh gave an initial C_D of 428.8 drag counts, whereas the aerodynamic analysis performed using the 16 millions cells mesh gave an initial C_D of only 367.9 drag counts. Therefore, there is a difference of more than 60 drag counts between the two meshes and this difference is present in the final C_D of the optimized configuration as well. This leads us to think that starting with a better mesh, or having more computational resources to use for this study, can lead us to have a final optimized configuration with a significantly lower C_D.

The fourth limitation is that structures is ignored in this study. In the truss-braced wing configuration, the coupling between aerodynamics and structures is one of the most distinctive features. For instance, knowing the stresses on the structural elements could make possible to further decrease the airfoil thicknesses. Therefore, an aerostructural optimization of the truss-braced wing configuration would allow us to make a more accurate comparison with the conventional configuration.

Notwithstanding all these issues, the present study can be considered a starting point for further truss-braced wing optimizations. Future work will involve addressing these limitations by improving the initial geometry, particularly near the junctions, including junction shape variables in the optimization, refining the mesh, and including structures in the optimization problem.

VI. Acknowledgments

The authors gratefully acknowledge support from NASA through award No. NNX14AC73A—Technical Monitor: Justin S. Gray. The computations required for this research were performed on the Flux HPC cluster at the University of Michigan Center of Advanced Computing. The authors would like to thank Dr. Gaetan K. W. Kenway for his help and the constructive suggestions, as well as our colleagues in the MDO Lab for numerous ideas.

References

[1] Zhang, K.-S., Ji, P.-B., Bakar, A., and Han, Z.-H., "Multidisciplinary evaluation of truss-braced wing for future green aircraft," *28th International Congress of the Aeronautical Sciences*, 2012.

[2] Gur, O., Bhatia, M., Schetz, J. A., Mason, W. H., Kapania, R. K., and Mavris, D. N., "Design Optimization of a Truss-Braced-Wing Transonic Transport Aircraft," *Journal of Aircraft*, Vol. 47, No. 6, 2010. doi:10.2514/1.47546.

[3] Gundlach, J. F., Tétrault, P.-A., Gern, F. H., Nagshineh-Pour, A. H., Ko, A., Schetz, J. A., Mason, W. H., Kapania, R. K., et al., "Conceptual design studies of a strut-braced wing transonic transport," *Journal of aircraft*, Vol. 37, No. 6, 2000, pp. 976–983.

[4] Grasmeyer, J. M., "Multidisciplinary design optimization of a transonic strut-braced wing aircraft," *AIAA*, Vol. 10, 1999, pp. 11–14.

[5] Hwang, J. T. and Martins, J. R. R. A., "GeoMACH: Geometry-Centric MDAO of Aircraft Configurations with High Fidelity," *Proceedings of the 14th AIAA/ISSMO Multidisciplinary Analysis Optimization Conference*, Indianapolis, IN, September 2012.

[6] Hwang, J. T., Kenway, G. K. W., and Martins, J. R. R. A., "Geometry and Structural Modeling for High-Fidelity Aircraft Conceptual Design Optimization," *Proceedings of the 15th AIAA/ISSMO Multidisciplinary Analysis and Optimization Conference*, Atlanta, GA, June 2014.

[7] Luke, E., Collins, E., and Blades, E., "A fast mesh deformation method using explicit interpolation," *Journal of Computational Physics*, Vol. 231, No. 2, 2012, pp. 586 – 601. doi:http://dx.doi.org/10.1016/j.jcp.2011.09.021.

[8] van der Weide, E., Kalitzin, G., Schluter, J., and Alonso, J., "Unsteady Turbomachinery Computations Using Massively Parallel Platforms," *Proceedings of the 44th AIAA Aerospace Sciences Meeting and Exhibit*, AIAA, Forth Worth, TX, 2006. doi:10.2514/6.2006-421.

[9] Knoll, D. A. and Keyes, D. E., "Jacobian-free Newton–Krylov methods: a survey of approaches and applications," *Journal of Computational Physics*, Vol. 193, No. 2, 2004, pp. 357–397.

[10] Spalart, P. R. and Allmaras, S. R., "A one-equation turbulence model for aerodynamic flows," 1992.

[11] Saad, Y. and Schultz, M. H., "GMRES: A generalized minimal residual algorithm for solving nonsymmetric linear systems," *SIAM Journal on scientific and statistical computing*, Vol. 7, No. 3, 1986, pp. 856–869.

[12] Gill, P., Murray, W., and Saunders, M., "SNOPT: An SQP Algorithm for Large-Scale Constrained Optimization," *SIAM Journal on Optimization*, Vol. 12, No. 4, 2002, pp. 979–1006. doi:10.1137/S1052623499350013.

[13] Perez, R. E., Jansen, P. W., and Martins, J. R. R. A., "pyOpt: a Python-based object-oriented framework for nonlinear constrained optimization," *Structural and Multidisciplinary Optimization*, Vol. 45, No. 1, 2012, pp. 101–118. doi:10.1007/s00158-011-0666-3.

[14] Bradley, M. K. and Droney, C. K., "Subsonic Ultra Green Aircraft Research phase II: N+4 Advanced Concept Development," Tech. rep., Boeing Research and Technology, May 2012, NASA/CR-2012-217556.

[15] Meadows, N. A., Schetz, J. A., Kapania, R. K., Bhatia, M., and Seber, G., "Multidisciplinary design optimization of medium-range transonic truss-braced wing transport aircraft," *Journal of Aircraft*, Vol. 49, No. 6, 2012, pp. 1844–1856.

[16] Gagnon, H. and Zingg, D. W., "High-Fidelity Aerodynamic Shape Optimization of Unconventional Aircraft Through Axial Deformation," *52nd Aerospace Sciences Meeting*, 2014, pp. 2014–0908.